**Key Points:**
- First realization of sea ice dynamics in tangent planes to the sphere
- Discretization of the sea ice dynamics in a three-dimensional Cartesian framework
- Realization of the sea ice dynamics in the ocean and sea ice model Icosahedral Non-hydrostatic-Ocean model

**Correspondence to:**
C. Mehlmann,
carolin.mehlmann@ovgu.de

# Discretization of Sea Ice Dynamics in the Tangent Plane to the Sphere by a CD-Grid-Type Finite Element

**Carolin Mehlmann[1]** and **Oliver Gutjahr[2,3]**

[1]Otto-von-Guericke University, Magdeburg, Germany, [2]Institut für Meereskunde, Universität Hamburg, Hamburg, Germany, [3]Max Planck Institute for Meteorology, Hamburg, Germany

**Abstract** We present a new discretization of sea ice dynamics on the sphere. The approach describes sea ice motion in tangent planes to the sphere. On each triangle of the mesh, the ice dynamics are discretized in a local coordinate system using a CD-grid-like non-conforming finite element method. The development allows a straightforward coupling to the C-grid like ocean model in Icosahedral Non-hydrostatic-Ocean model, which uses the same infrastructure as the sea ice module. Using a series of test examples, we demonstrate that the non-conforming finite element discretization provides a stable realization of large-scale sea ice dynamics on the sphere. A comparison with observation shows that we can simulate typical drift patterns with the new numerical realization of the sea ice dynamics.

**Plain Language Summary** Sea ice in polar regions plays an important role in the exchange of heat and freshwater between the atmosphere and the ocean and hence for climate in general. Therefore climate models require a description (a set of equations) to express the large-scale sea ice motion. We present a mathematical framework for describing sea ice flow in a global three-dimensional Cartesian system. The idea is to express the sea ice motion in tangent planes. In this reference system, we solve the mathematical equations that describe the sea ice motion. The equations are approximated on a computational grid, that consists of triangles covering the surface of the sphere. On each triangle the sea ice velocity is placed at the edge midpoint. The development is motivated by the infrastructure of the ocean and sea ice model Icosahedral Non-hydrostatic-Ocean model. The old representation of sea ice dynamics uses a different design principle. Therefore, the communication between the sea ice and ocean model is computationally expensive. To circumvent this problem we have developed a numerical realization of sea ice dynamics that uses the same infrastructure as the ocean model. We show that the new realization of the sea ice dynamics is capable of capturing the sea ice drift.

## 1. Introduction

Sea ice is an important component of the climate system, regulating the exchange of heat, momentum, and moisture between the atmosphere and the polar oceans (Stroeve & Notz, 2018). Freezing, drifting, and melting of sea ice further redistributes salt and freshwater in the ocean. During drift, sea ice deforms in response to wind and ocean forcing, modifying its thickness by forming pressure ridges or areas of open water. Modeling complex ice drift presents a number of challenges. In addition to the representation of physical processes, the numerical discretization of sea ice dynamics on the model grid is particularly challenging.

For example, the *Icosahedral Non-hydrostatic-Ocean model* (ICON-O, Korn, 2017) uses a triangular grid created by refining an icosahedrons. For each triangle, a local coordinate system is defined that is embedded in a three-dimensional Cartesian system. Sea ice dynamics are part of the ocean model, but follow a different design principle. This discrepancy leads to a numerical overload and projection errors when the different model components are coupled (Jungclaus et al., 2021). We introduce a discretization of sea ice dynamics on the sphere that differs from common approaches in sea ice modeling and allows straightforward coupling with ICON-O.

In most climate models, sea ice dynamics are discretized in spherical coordinates on rectangular curvilinear grids, with pole singularities smoothly shifted to nearby land masses (Hunke & Dukowicz, 2002). However, discretizing the sphere with rectangular orthogonal grids can lead to a non-uniformity of the mesh. There exist different approaches to circumvent this shortcoming, for example, by using a cubed sphere, a multi-polar grid, or an unstructured grid (Comblen et al., 2009). The use of unstructured grids poses a variety of challenges for the model realization and requires the development of new approaches to discretize the partial differential equations that describe sea ice dynamics.

The development of global ocean models based on unstructured grids has made substantial progress in recent years. Examples for this initiatives are the *Finite-Volume Sea Ice–Ocean model* (FESOM, Wang et al., 2014; Danilov et al., 2017), the *Model for Prediction Across Scales* (MPAS, Ringler et al., 2013; Petersen et al., 2019) and ICON-O (Korn, 2017). In the case of ICON-O, the ocean model and the sea ice module use a different infrastructure. The ocean model is formulated on the sphere using local coordinate systems embedded into a three-dimensional Cartesian framework. However, the sea ice dynamics are currently discretized in spherical coordinates on a rotated grid, based on the sea ice module of FESOM. Furthermore, ICON-O applies an analog of an Arakawa C-grid, while the sea ice module of FESOM uses an Arakawa A-grid type staggering. Therefore, an interpolation, rotation and transformation of the sea ice, ocean, and atmospheric variables is required to couple the sea ice module to the ocean model. Besides the computational overhead, the projection of the approximations between the sea ice module of FESOM and ICON-O introduces numerical errors (Jungclaus et al., 2021).

We aim to develop a numerical framework for sea ice dynamics in ICON-O that uses the same coordinate system and staggering as the ocean model. Specifically, we address the problem of how to formulate sea ice dynamics on a sphere embedded in a three-dimensional Cartesian framework with a direct coupling to a C-grid ocean model. The discretization is realized by formulating the sea ice dynamics in tangent planes, and approximating it with a CD-grid-like finite element. The CD-grid-type discretization is capable of simulating sea ice drift (Lietaer et al., 2008; Mehlmann & Korn, 2021) and offers appealing resolution properties in addition to a straightforward coupling to the C-grid ocean (Mehlmann et al., 2021).

The triangular mesh in ICON-O is generated by refining an icosahedron and projecting it onto the surface of the sphere. An efficient way to simulate sea ice dynamics with the CD-grid element in the tangent plane to the sphere is to establish local reference frames on each flat triangle (Comblen et al., 2009). By realizing the discretization on flat triangles we approximate the sea ice flow on the spherical surface with the sea ice motion on a refined icosahedrons. The CD-grid-like approximation is a suitable approach since it is of first order, while the geometric error between the icosahedron and the sphere is of second order (Guo, 2020).

A discretization of the shallow water equation with the CD-grid-type finite element using flat triangles as an approximation of the sphere has been used by Comblen et al. (2009). In the article, the authors relate a local coordinate system defined on flat triangles to a nodal coordinate framework. The finite element system matrix, which is assembled in the local coordinate system, is transformed into a nodal framework such that a global algebraic system is obtained. In contrast to the shallow water equation, the sea ice momentum equations consist of the divergence of the symmetric strain rate tensor, which implies that the vector Laplacian of the symmetric tensor needs to be approximated with sufficient accuracy. Furthermore, the CD-grid-like finite element discretization of sea ice momentum equation requires a stabilization (Mehlmann & Korn, 2021). We present a matrix-free approach that defines the tangential operators with respect to the already existing three-dimensional Cartesian infrastructure in ICON-O. In more detail, we discuss how the planar CD-grid formulation presented by Mehlmann and Korn (2021) is realized in the local coordinate system embedded in the three-dimensional Cartesian frame. We demonstrate that the discretization is a suitable approach to represent the divergence of the strain rate tensor and show that the new discretization in ICON-O robustly approximates the large-scale sea ice motion.

The remainder of the manuscript is structured as follows. Section 2 introduces the viscous-plastic (VP) sea ice dynamics and briefly presents the concept of the covariant derivative. Section 3 outlines the spatial discretization of the sea ice drift in a local reference system related to the three-dimensional infrastructure in ICON-O. The numerical analysis is presented in Section 4. The paper closes with a discussion and conclusion in Section 5.

## 2. Model Description

For simplicity, we formulate the sea ice flow in a two-dimensional Cartesian coordinate system. The motion is expressed as

$$m\partial_t \mathbf{v} + m f_c \mathbf{e}_z \times \mathbf{v} = \mathrm{div}\,\boldsymbol{\sigma} + a\mathbf{F}(\mathbf{v}) - mg\nabla H, \tag{1}$$

$$\partial_t \mathbf{h} + \mathrm{div}(\mathbf{v}\mathbf{h}) = 0, \tag{2}$$

**Table 1**
*Physical Parameters of the Sea Ice Momentum Equation*

| Parameter | Definition | Value |
|---|---|---|
| $\rho_{ice}$ | Sea ice density | $900 \text{ kg m}^{-3}$ |
| $\rho_a$ | Air density | $1.3 \text{ kg m}^{-3}$ |
| $\rho_w$ | Water density | $1{,}026 \text{ kg m}^{-3}$ |
| $C_a$ | Air drag coefficient | $1.2 \cdot 10^{-3}$ |
| $C_w$ | Water drag coefficient | $5.5 \cdot 10^{-3}$ |
| $f_c$ | Coriolis parameter | $1.46 \cdot 10^{-4} \text{ s}^{-1}$ |
| $P^\star$ | Ice strength parameter | $27.5 \cdot 10^3 \text{ N m}^{-2}$ |
| $C$ | Ice concentration parameter | $20$ |
| $e$ | Ellipse aspect ratio | $2$ |

where $m = \rho_{ice}h_{ice} + \rho_{snow}h_{snow}$ is the total mass, with sea ice thickness and density, $h_{ice}$, $\rho_{ice}$, as well as the snow thickness and density $h_{snow}$, $\rho_{snow}$. $f_c$ describes the Coriolis parameter, $g$ is the gravitational acceleration, $H$ is the sea surface elevation, and $e_z$ is the vertical ($z$-direction) unit vector. The tracers are collected in the vector

$$\mathbf{h} = (h_{ice}, h_{snow}, a),$$

where $a$ with the restriction $a \leq 1$ is the sea ice concentration. The forcing term $\mathbf{F}(\mathbf{v})$ is the sum of the ocean and atmospheric surface stresses

$$\mathbf{F}(\mathbf{v}) = C_w \rho_w |\mathbf{v}_w - \mathbf{v}|_2 (\mathbf{v}_w - \mathbf{v}) + C_a \rho_a |\mathbf{v}_a|_2 \mathbf{v}_a, \tag{3}$$

with the ocean velocity $\mathbf{v}_w$ and the wind velocity $\mathbf{v}_a$. The internal stresses in the ice $\boldsymbol{\sigma}$ are modeled by the VP sea ice rheology (Hibler, 1979).

The nonlinear VP rheology relates the stress tensor $\boldsymbol{\sigma}$ to the strain rate tensor

$$\dot{\epsilon} = \frac{1}{2}\left(\nabla\mathbf{v} + \nabla\mathbf{v}^T\right), \quad \dot{\epsilon}' = \dot{\epsilon} - \frac{1}{2}\text{tr}(\dot{\epsilon})I, \tag{4}$$

by the following constitutive law

$$\boldsymbol{\sigma} = 2\eta\dot{\epsilon}' + \zeta \, \text{tr}(\dot{\epsilon}) \, I - \frac{P_{ice}}{2} I, \tag{5}$$

where $I$ is the identity matrix. The viscosities, $\eta$ and $\zeta$, are given by $\eta = e^{-2}\zeta$, and

$$\zeta = \frac{P_0}{2\Delta(\dot{\epsilon})}, \quad \Delta(\dot{\epsilon}) = \sqrt{\frac{2}{e^2}\dot{\epsilon}' : \dot{\epsilon}' + \text{tr}(\dot{\epsilon})^2 + \Delta_{\min}^2}. \tag{6}$$

$\Delta_{\min} = 2 \cdot 10^{-9} \text{ s}^{-1}$ is the threshold that describes the transition between the viscous and the plastic regimes. The eccentricity, $e = 2.0$, of the elliptic yield curve determines the stress states in the plastic regime. $\dot{\epsilon}' : \dot{\epsilon}'$ denotes the inner product of the two tensors. Following Kreyscher et al. (2000), the replacement pressure $P_{ice}$ and the ice strength $P_0$ in Equation 5 are expressed as

$$P_{ice} = P_0 \frac{\Delta}{(\Delta + \Delta_{\min})}, \quad P_0(h_{ice}, a) = P^\star h_{ice} \exp\left(-C(1 - a)\right), \tag{7}$$

with $P^\star = 27.5 \cdot 10^3 \text{ N m}^{-2}$ and the constant $C = 20$. An overview of all parameters is given in Table 1.

Traditionally, sea ice dynamics models have been formulated and used in two-dimensional Cartesian coordinates for simplicity. However, sea ice flow takes place on a spherical manifold and is realized in many climate models in spherical curvilinear coordinates. Using curvilinear coordinates, the local derivatives produces so-called metric terms, which derive from the curvature of the grid (Hunke & Dukowicz, 2002). The metric terms ensure that the sea ice flow only takes place within the spherical manifold. In the framework of curvilinear coordinates, the considered domain as well as the sea ice velocity are two-dimensional objects which allows a straightforward discretization.

In the three-dimensional Cartesian system used in ICON-O the two-dimensional sea ice flow can be described by tangential vector fields. We assume that the sea ice drift $\tilde{\mathbf{v}}$ three dimensional Cartesian vector. In each point $\mathbf{x}(x, y, z) \in \Gamma$ of the surface, the horizontal sea ice velocity can be represented by

$$\mathbf{v}(\mathbf{x}) := B\tilde{\mathbf{v}}(\mathbf{x}) \tag{8}$$

with the transformation matrix

$$B = e_1\boldsymbol{\tau}^T + e_2\mathbf{n}^T + e_3\boldsymbol{r}^T. \tag{9}$$

The superscript $T$ is the transpose. $\mathbf{n}(\mathbf{x})$ and $\boldsymbol{\tau}(\mathbf{x})$ are the two linearly independent tangential vectors spanning the tangent plane $M_{\mathbf{x}}$. $\boldsymbol{r}(\mathbf{x})$ is the outward pointing radial vector and $e_1$, $e_2$, $e_3$ are the unit vectors spanning $\mathbb{R}^3$.
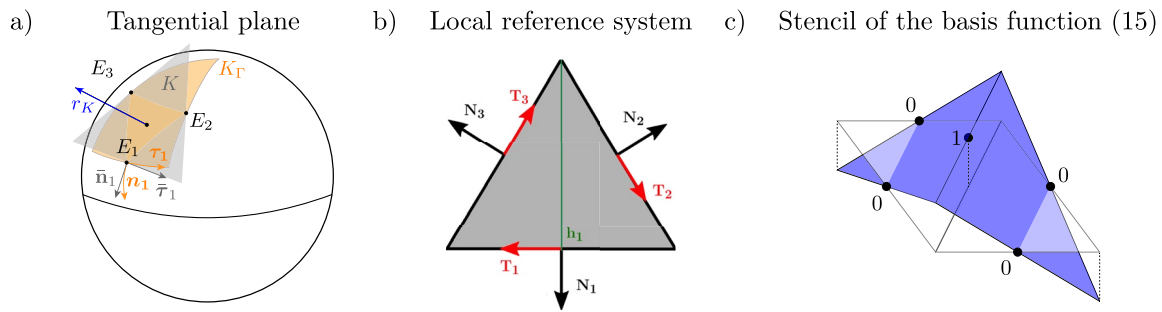
**Figure 1.** (a) Tangent plane (gray) defined through the edge midpoints $E_1$, $E_2$, $E_3$ of a curved triangle (yellow), which is assigned to the surface of the sphere. (b) On each triangle we assign a local reference system with basis $\mathbf{N}_1$ and $\mathbf{T}_1$. $h_1$ is the height of triangle defined at edge $E_1$. (c) Coupling of the Crouzeix-Raviart basis function at an edge.

Note that the symbol $:=$ in Equation 8 stands for *defined as*. Based on the transformation (9), a Cartesian vector is represented in the coordinate system spanned by $\tau$, $\mathbf{n}$, $r$. An illustration of the tangent plane is given in the left panel of Figure 1.

For the definition of derivatives in tangent planes a special concept is needed, the so-called *covariant derivatives*. On the surface of the sphere, the covariant derivative coincides with the orthogonal projection of the directional derivative of a tangential vector field. Let $P$ be the orthogonal projection onto the surface

$$P = \left(I - r(\mathbf{x})r(\mathbf{x})^T\right). \tag{10}$$

The directional derivative of a tangential field $\tilde{\mathbf{v}}$ in direction $P\tilde{\mathbf{u}}$ is expressed as

$$(P\tilde{\mathbf{u}} \cdot \nabla)\,\tilde{\mathbf{v}} := \nabla\tilde{\mathbf{v}}P\tilde{\mathbf{u}},$$

with $\nabla\tilde{\mathbf{v}} \in \mathbb{R}^{3\times3}$. Note that $\tilde{\mathbf{u}}$ is a function at the surface of the sphere and both vectors, $\tilde{\mathbf{u}}$ and $\tilde{\mathbf{v}}$, are expressed with respect to the basis of $\mathbb{R}^3$. Then the projection of $\nabla\tilde{\mathbf{v}}P\tilde{\mathbf{u}}$ into the tangent plane is

$$P^T\nabla\tilde{\mathbf{v}}P\tilde{\mathbf{u}}.$$

Please note that $P$ is symmetric. Considering the covariant derivative in direction of the basis vectors $e_1$, $e_2$, $e_3$ of $\mathbb{R}^3$, we obtain the partial derivative of $\tilde{\mathbf{v}}$.

Using the transformation (9), we can express the derivative by only four components instead of nine, which is appealing in terms of numerical efficiency.

$$\nabla\mathbf{v} = BP\nabla\mathbf{v}P^T B^T, \quad \nabla\mathbf{v} = \begin{pmatrix} (\nabla\mathbf{v})_{11} & (\nabla\mathbf{v})_{12} & 0 \\ (\nabla\mathbf{v})_{21} & (\nabla\mathbf{v})_{22} & 0 \\ 0 & 0 & 0 \end{pmatrix}, \tag{11}$$

where the projection $BP$ is

$$BP = \left(I - rr^T\right)B = e_1\tau^T + e_2\mathbf{n}^T. \tag{12}$$

Based on the concept of the covariant derivative in Equation 11, we derive an efficient numerical representation in Section 3.

## 3. Spatial Discretization

In this section, we introduce a finite element approach for sea ice dynamics in tangent planes to the sphere. The approach is realized on an unstructured triangular grid that discretizes the surface of the Earth. We start with outlining the weak formulation of the momentum equation, which forms the basis of the finite element discretization:

$$\int_S (m\partial_t \tilde{\mathbf{v}} + f_c e_z \times \tilde{\mathbf{v}}) \boldsymbol{\phi} \, ds = - \int_S \boldsymbol{\sigma} : \nabla_\Gamma \boldsymbol{\phi} \, ds + \int_S (a\mathbf{F}(\tilde{\mathbf{v}}) - mg\nabla_\Gamma H) \boldsymbol{\phi} \, ds, \tag{13}$$

with

$$\nabla_\Gamma \boldsymbol{\phi} = P^T \nabla \boldsymbol{\phi} P \in \mathbb{R}^{3\times 3}.$$

The surface gradient of the scalar $H$ is given by

$$\nabla_\Gamma H = P \nabla H.$$

Note that the weak formulation is achieved by multiplying the momentum equation with a test function and integrating the different terms over the ice covered domain $S$ which is a subset of the surface of the sphere. The rheology term is reformulated by applying integration by parts and assuming no slip boundary conditions. $\boldsymbol{\sigma} : \nabla_\Gamma \boldsymbol{\phi}$ denotes the inner product of the two tensors.

The finite element method is an excellent candidate to discretize the sea ice flow in tangent planes to the sphere. Usually finite elements are applied by establishing a local coordinate system for each grid cell (element). By approximating the sea ice flow on flat triangles instead of curved ones, we can interpret the flat element as a tangent plane. In our case the tangent plane is defined by the edge midpoints of the curved triangle, see Figure 1. On the supporting plane of the flat triangle, we define a local coordinate system and represent a discrete vector field by edge integration through the CD-grid-like non-conforming piecewise-linear finite element (Crouzeix & Raviart, 1974), the so called Crouzeix-Raviart element.

In following we outline how this idea is realized in ICON-O. More in detail we describe the construction of tangential operators in a two-dimensional reference framework in relation to the three-dimensional infrastructure of ICON-O. The reference system is achieved by projecting the already existing three-dimensional tangential surface vectors (defined at edge midpoints) into the flat triangles and transforming them.

In what follows, we focus on discretization of the vector Laplacian in its weak from, $(\nabla \mathbf{v} + \nabla \mathbf{v}^T, \nabla \boldsymbol{\phi})$, since this is the most difficult part. According to the representation of the covariant derivative in Equation 11, we compute the derivative of the vector field in a tangent plane, which is realized by a flat triangle. Therefore, we assign to each curved triangle $K_\Gamma$ on the surface a flat triangle $K$ that coincides with the curved triangle at edge midpoints. An example is shown in Figure 1. A key element of covariant derivatives is the orthogonal projection into the tangent plane (10), which requires the description of an outward pointing radial vector $r^K$. Using the edge midpoints $E_1$, $E_2$, $E_3$ of the curved triangle, we define $\boldsymbol{r}^K$ as

$$\boldsymbol{r}^K = \frac{1}{3} \frac{E_1 + E_2 + E_3}{|E_1 + E_2 + E_3|}.$$

The grid used in ICON-O provides three-dimensional tangential surface vectors $(\mathbf{n}_i, \boldsymbol{\tau}_i)$ in each edge midpoint $E_i$. We make use of this infrastructure and project the tangential surface vectors into the plane by

$$\bar{\mathbf{n}}_i^K = \frac{P\mathbf{n}_i}{|P\mathbf{n}_i|}, \quad \bar{\boldsymbol{\tau}}_i^K = \frac{P\boldsymbol{\tau}_i}{|P\boldsymbol{\tau}_i|}. i = 1, .., 3,$$

where P is the orthogonal projection defined in Equation 10. $\mathbf{n}_i$ and $\boldsymbol{\tau}_i$ are the vectors normal and tangential to edge which belongs to $E_i$. A sketch of the projected vectors is shown in the left panel of Figure 1. Analogously to Equation 9, we transform the projected vectors $\bar{\mathbf{n}}_i^K$, $\bar{\boldsymbol{\tau}}_i^K$ into the reference system associated with the respective plane triangle $K$.

$$B_K = e_1 (\boldsymbol{\tau}^K)^T + e_2 (\mathbf{n}^K)^T + e_3 (\boldsymbol{r}^K)^T \tag{14}$$

To simplify the notation, we express the normal and tangential vectors of the reference system (middle panel in Figure 1) as

$$\mathbf{N}_i^K := B_K \bar{\mathbf{n}}_i^K, \quad \mathbf{T}_i^K := B_K \bar{\boldsymbol{\tau}}_i^K.$$

The normal and tangential reference vectors have the form

$$\mathbf{N} = (N^x, N^y, 0), \quad \mathbf{T} = (T^x, T^y, 0),$$

and allows us to compute the gradient by only four components, see Equation 12. The vectors $\mathbf{N}$, $\mathbf{T}$ are initialized once at the beginning of a simulation.

When calculating on the flat triangle instead of the curved one, a geometrical error is introduced. Since we are using low-order finite elements, the geometrical error is balanced with the discretization error introduced by the finite element approximation. Therefore, it is sufficient to use flat triangles when linear finite elements are applied (Comblen et al., 2009; Guo, 2020).

On each flat triangle $K$ we define three Crouzeix-Raviart basis functions. The space of the Crouzeix-Raviart functions consists of the piecewise linear functions that are continuous at the edge midpoints of a triangle. The coupling of two Crouzeix-Raviart basis functions is presented in the right panel in Figure 1. In each edge midpoint $E_i$, $i = 1, 2, 3$ of a triangle $K$ the linear finite element basis function is given as

$$\phi_i|_K(E_j) = \delta_{ij}, \quad \forall i, j = 1, .., 3. \tag{15}$$

The derivative of the basis function is

$$\partial_{\mathbf{N}_i} \phi_i|_K = \frac{2}{h_i}, \quad \partial_{\mathbf{T}_i} \phi_i|_K = 0, \tag{16}$$

where $h_i$ is the height orthogonal to the edge $e_i$ with the midpoint $E_i$. On a triangle $K$, the discrete sea ice velocity is expressed as

$$\mathbf{v}_h|_K = \sum_{i=1}^{3} \left( v_i \mathbf{N}_i^K + u_i \mathbf{T}_i^K \right) \phi_i, \tag{17}$$

with the scalar coefficients $u_i$ and $v_i$. For better readability, we omit the superscript $K$ of the projected normal and tangential vectors $\mathbf{N}_i^K$ and $\mathbf{T}_i^K$ in the following. Using the relation (16), the gradient of $\mathbf{v}_h$ on $K$ and its transpose are given by

$$\begin{aligned}
\nabla \mathbf{v}_h|_K &= \sum_{i=1}^{3} (v_i \mathbf{N}_i + u_i \mathbf{T}_i) \nabla^T \phi_i = \sum_{i=1}^{N} (v_i \mathbf{N}_i + u_i \mathbf{T}_i) \mathbf{N}_i^T \partial_n \phi_i, \\
\nabla \mathbf{v}_h^T|_K &= \sum_{i=1}^{3} \nabla \phi_i \left( v_i \mathbf{N}_i^T + u_i \mathbf{T}_i^T \right) = \sum_{i=1}^{N} \mathbf{N}_i \partial_n \phi_i \left( v_i \mathbf{N}_i^T + u_i \mathbf{T}_i^T \right),
\end{aligned} \tag{18}$$

where the superscript $T$ indicates the transpose. Analogous to the discrete velocity, we decompose the test function and the gradient of the test function into a normal and a tangential component
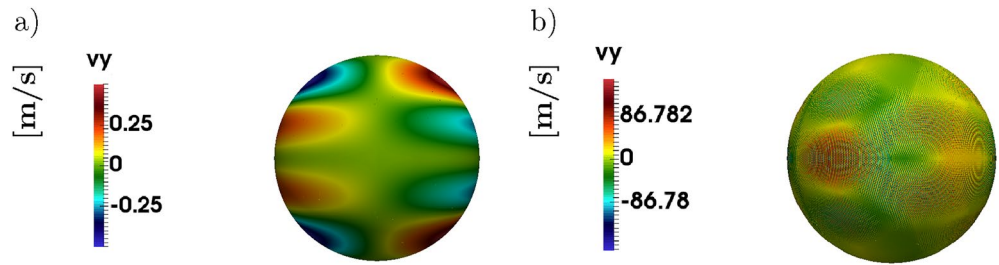
$$\boldsymbol{\phi}|_K = \sum_{j=1}^{3} \mathbf{N}_j \phi_j^n + \mathbf{T}_j \phi_j^\tau, \quad \nabla \boldsymbol{\phi}|_K = \sum_{j=1}^{3} \mathbf{N}_j \mathbf{N}_j^T \partial_n \phi_j^n + \mathbf{T}_j \mathbf{N}_j^T \partial_n \phi_j^\tau. \tag{19}$$

A direct discretization of the VP sea ice model with Crouzeix-Raviart elements would lead to an oscillation in the velocity field (Mehlmann & Korn, 2021). Therefore, the following stabilized momentum equation is considered:

$$\sum_K \sum_{j=1}^{3} \int_K m(\partial_t \mathbf{v}_h - F(\mathbf{v}_h) + mg\nabla H) \boldsymbol{\phi}_j + \int_K \boldsymbol{\sigma}_h : \nabla \boldsymbol{\phi}_j - \sum_e \sum_{j=1}^{N} S_j^e(\mathbf{v}_h, \boldsymbol{\phi}) = 0, \tag{20}$$

where the stabilization term is given as

$$S_j^e(\mathbf{v}_h, \boldsymbol{\phi}) := 2\zeta_e \frac{\alpha}{|e|} \int_e \left[ \mathbf{v}_{e_i} \right] \left[ \boldsymbol{\phi}_{e_j} \right] ds. \tag{21}$$

**Figure 2.** Effect of stabilization on sea ice velocity calculated with the simplified moment Equation 23. (a) Second component $\mathbf{v}^y$ of the sea ice velocity with stabilization (21). (b) Second component $\mathbf{v}^y$ computed without stabilization.

Here $[\mathbf{v}_h]$ denotes a jump of the velocity at an edge $e$ defined by

$$[\mathbf{v}_h] := \mathbf{v}_h^+ - \mathbf{v}_h^-, \quad \mathbf{v}_h^\pm := \lim_{\epsilon \downarrow 0} \mathbf{v}_h^\pm(x \pm \epsilon \mathbf{n}). \tag{22}$$

The stabilization term can be interpreted as a penalization of the cross element jumps of the sea ice velocity. A detailed description of the stabilization can be found in Mehlmann and Korn (2021).

To solve Equation 20 for discrete velocity components $u_i$, $v_i$, we need to compute several integrals as described by Mehlmann and Korn (2021). Note that the normal and tangential vectors $\mathbf{N}^K$ and $\mathbf{T}^K$ must be setup explicitly only for the calculation of the spatial derivatives.

## 4. Numerical Evaluation

This section presents a numerical analysis of the new realization of sea ice dynamics on the sphere. In Section 4.1, the numerical convergence of strain rate tensor is analyzed to show that the approach is a suitable approximation of the vector Laplacian. In Section 4.2, an idealized box test is evaluated to demonstrate the robustness of the new approach. Finally, in Section 4.3 we compare the simulated sea ice drift from ICON-O with observations.

### 4.1. Strain Rate Tensor

We consider the following simplified model of the sea ice momentum Equation 1

$$-\text{div}(\boldsymbol{\sigma}) + \frac{1}{100}\mathbf{v} = rhs, \tag{23}$$

and express the VP stress tensor in the viscous regime as

$$\boldsymbol{\sigma} = \zeta \frac{1}{2}\left(\nabla\mathbf{v} + \nabla\mathbf{v}^T\right), \quad \zeta = \frac{P(h_{ice}, a)}{\Delta_{\min}}, \quad h_{ice} = 2, \quad a = 1.$$

We keep the sea ice thickness and sea ice concentration constant. The simplified model is solved on the surface of the sphere with a radius $R = 6.371229 \cdot 10^6$ m. For a given analytic solution

$$\mathbf{v}^* = \begin{pmatrix} \sin\left(10^{-6}Ry\right) \\ 0 \\ 0 \end{pmatrix},$$

the right hand side is given as $rhs = -\text{div}\left(\frac{1}{2}\zeta\left(\nabla\mathbf{v}^* + \nabla\mathbf{v}^{*T}\right)\right) + \frac{1}{100}\mathbf{v}^*$.

We solve Equation 23 with the Conjugate Gradient method. The velocity field in the right plot in Figure 2 shows instabilities. These instabilities arise from the discretization of the strain rate tensor, $\nabla\mathbf{v}_h + \nabla\mathbf{v}_h^T$ with the Crouzeix-Raviart element. The discretized strain rate tensor has a nontrivial kernel, even when rigid body rotations are removed, see Falk (1991) or Mehlmann and Korn (2021).
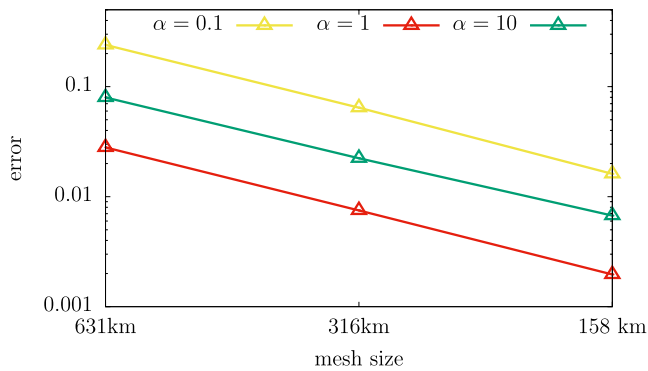
**Figure 3.** Discretization error of the second component of sea ice velocity for different stabilization parameters $\alpha$ (21) evaluated in the maximums norm (24).

By applying stabilization (21) with $\alpha = 1.0$ these oscillations vanish. To address the effect of the stabilization parameter $\alpha$ in Equation 21, we analyze the numerical convergence for different choices of $\alpha$. For this purpose meshes with equilateral triangles with a side length of 631, 316 and 158 km are used. We evaluate the error in maximums norm, which is defined as

$$e_r = \max_{i=1,\dots,N} |\mathbf{v}^i - \mathbf{v}^i_{\text{analytic}}|, \quad i = 1 \dots N. \tag{24}$$

Figure 3 shows the approximation error evaluated in the second component of the velocity for $\alpha = 0.1, 1, 10$. The error reduces linearly with increased spatial resolution and is larger for $\alpha \neq 1.0$. This result is in agreement with findings of Hansbo and Larson (2003), where the authors discretized a linear elasticity problem with the Crouzeix-Raviart finite element. The conclusion is further supported since $\alpha = 0.1$ produces only a small oscillation in the simulated velocity field, while $\alpha = 10$ over damps the approximation (results are not shown).

## 4.2. The Viscous-Plastic Sea Ice Model

To analyze the robustness of the new discretization, we solve the VP sea ice momentum equation on the sphere and compare the results to a simulation conducted in two-dimensional planar geometry. For the analysis, an idealized test case used, which was already used by Mehlmann and Korn (2021). The test case is a slightly modified version of the box test used by Danilov et al. (2015) and Hunke and Dukowicz (2002).

We consider a squared domain of length $L = 1,024$ km and assume Dirichlet boundary conditions. For simplicity, we neglect the Coriolis force and sea surface tilt term. The sea ice motion is described by

$$\rho_{ice} h_{ice} \partial_t \mathbf{v} = \text{div}(\boldsymbol{\sigma}) + \rho_w C_w |\mathbf{v}_w - \mathbf{v}|_2 (\mathbf{v}_w - \mathbf{v}) + \rho_a C_a |\mathbf{v}_a|_2 \mathbf{v}_a. \tag{25}$$

Following Hunke (2001) and Danilov et al. (2015), we defined the ocean velocity as

$$\mathbf{v}_w^x = \frac{0.1(2y - L)}{L}, \quad \mathbf{v}_w^y = \frac{0.1(L - 2x)}{L}.$$

The wind velocity is given by

$$\mathbf{v}_a^x = 5 + (\sin(2\pi t/4) - 3)(\sin(2\pi x/L)\sin(2\pi y/L),$$

$$\mathbf{v}_a^y = 5 + (\sin(2\pi t/4) - 3)(\sin(2\pi y/L)\sin(2\pi x/L).$$

We use the same forcing on the sphere and the planar domain. The initial ice velocity is $\mathbf{v}(t_0) = 0$. The sea ice thickness and concentration is constant with $h_{ice} = 2$m and $a = \frac{x}{L}$.
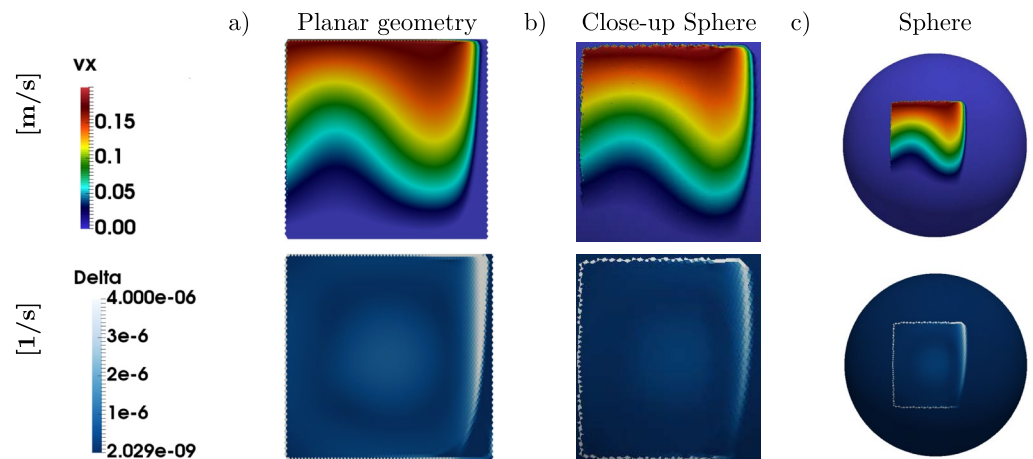
In Figure 4 the sea ice velocity and the total deformation $\Delta(\dot{\epsilon})$ is presented. Both variables behave qualitatively similar on the sphere and in the planar case. We attribute the slight differences to the curvature in the spherical setup.

## 4.3. Sea Ice Dynamics in ICON-O

In this section we demonstrate that the new sea ice dynamics are able to reproduce typical sea ice drift patterns. Therefore, we perform realistic simulations using ICON-O (Korn et al., 2022) on a uniform 40 km (r2b6) grid with 64 vertical $z$-levels and a time step of 30 min. We first produce a spin-up run with the old sea ice dynamics. Both sea ice models are based on an EVP formulation with 120 subiterations. Details on the numerical realization of the old model (sea ice module of FESOM) are given in Danilov et al. (2015), whereas information on the new sea ice module can be found in Mehlmann and Korn (2021).

This experiment is initialized with averaged temperature and salinity values from 1979 to 1993 from Polar Science Center Hydrographic Climatology (PHC3.0, Steele et al., 2001) and forced by a three-hourly atmospheric reanalysis from the Japanese 55-year atmospheric reanalysis to drive ocean-sea ice models version 1.4.0 (JRA55-do,

**Figure 4.** Comparison of the sea ice velocity and the total deformation computed with an idealized test case on a 1,024 km² domain (25). (Left column) First component of the sea ice velocity, $\mathbf{v}^x$, and the total deformation, $\Delta(\dot{\epsilon})$, calculated on planar geometry. (Right column) $\mathbf{v}^x$ and $\Delta(\dot{\epsilon})$ computed on the sphere. (Middle column) A close up of the computational domain on the sphere.

Tsujino et al., 2018) for the period from January 1958 to March 2018. The JRA55-do reanalysis has a horizontal resolution of about 55 km. Surface fluxes over ocean and sea ice are calculated with bulk formulas according to Large and Yeager (2009). The initial and the forcing fields are bilinearly interpolated onto the ICON-O grid.

Based on the spin-up, we perform a second experiment using the new sea ice dynamics. The initial state is derived from output of the spin up run for 1 January 2018. We run the second experiment until March 2018. Since the focus of this work is to evaluate the new dynamics, we concentrate on these three winter months.

The thermodynamics of the sea ice module are realized by a single-category, zero-layer formulation (Semtner, 1976). The description of the thermodynamics has been adopted from the MPI-OM (Notz et al., 2013). Because sea ice is embedded in the ocean, the thickness must be limited when using $z$-levels with only a free sea surface. We set the maximum ice thickness in both simulations to 80% of the thickness of the first vertical layer of the ocean model, which roughly corresponds to an ice thickness of 10 m (the first layer of the ocean model is 12 m thick). This constraint does not affect our assessment, as the ice thickness remains well below this threshold (not shown).

We compare the simulated sea ice drift from both ICON-O experiments to National Snow and Ice Data Center (NSIDC) sea ice drift data from January–March 2018, which have a resolution of 25 km. The sea ice extent is compared to data from the EUMETSAT Ocean and Sea Ice Satellite Application Facility (OSI SAF v2, Lavergne et al., 2019). For comparison, we interpolate all data sets by nearest neighbor to a regular grid with a horizontal resolution of 50 km.

Figure 5 shows the 10 m wind forcing from JRA55-do, averaged over January–March 2018, and the mean sea ice drift from NSDIC and the two ICON-O experiments for the same period. The sea ice drift in both ICON-O experiments closely follows the wind forcing and the ice moves anticyclonally in the Beaufort Sea. Compared to NSIDC, sea ice drift is slower overall in both ICON-O simulations. In the Chuchki Sea, the drift pattern of both ICON-O simulations deviates from NSIDC. The pattern is unrelated to the wind forcing as the wind direction from JRA55-do match that of the National Centers for Environmental Prediction (NCEP) reanalysis 1, which is used for NSIDC (not shown). This drift deviation could indicate an offset in the wind direction in the reanalysis, a too weak ocean circulation in ICON-O, or deviations due to data assimilation in the NSIDC data.

Along the ice edges, the drift in ICON-O is faster with the old than with the new sea ice dynamics. This behavior results from the coupling of the wind and ocean stress. As suggested by Connolley et al. (2004), the coupling in the new dynamics weight the wind and ocean stresses with the sea ice concentration (term $a\mathbf{F}(\mathbf{v})$ in Equation 1). In contrast, the coupling in the old dynamics considers the full wind and ocean stresses. This effect is best observed along the ice edge in the Greenland Sea, where both simulations produce an ice cover that extends too far south.
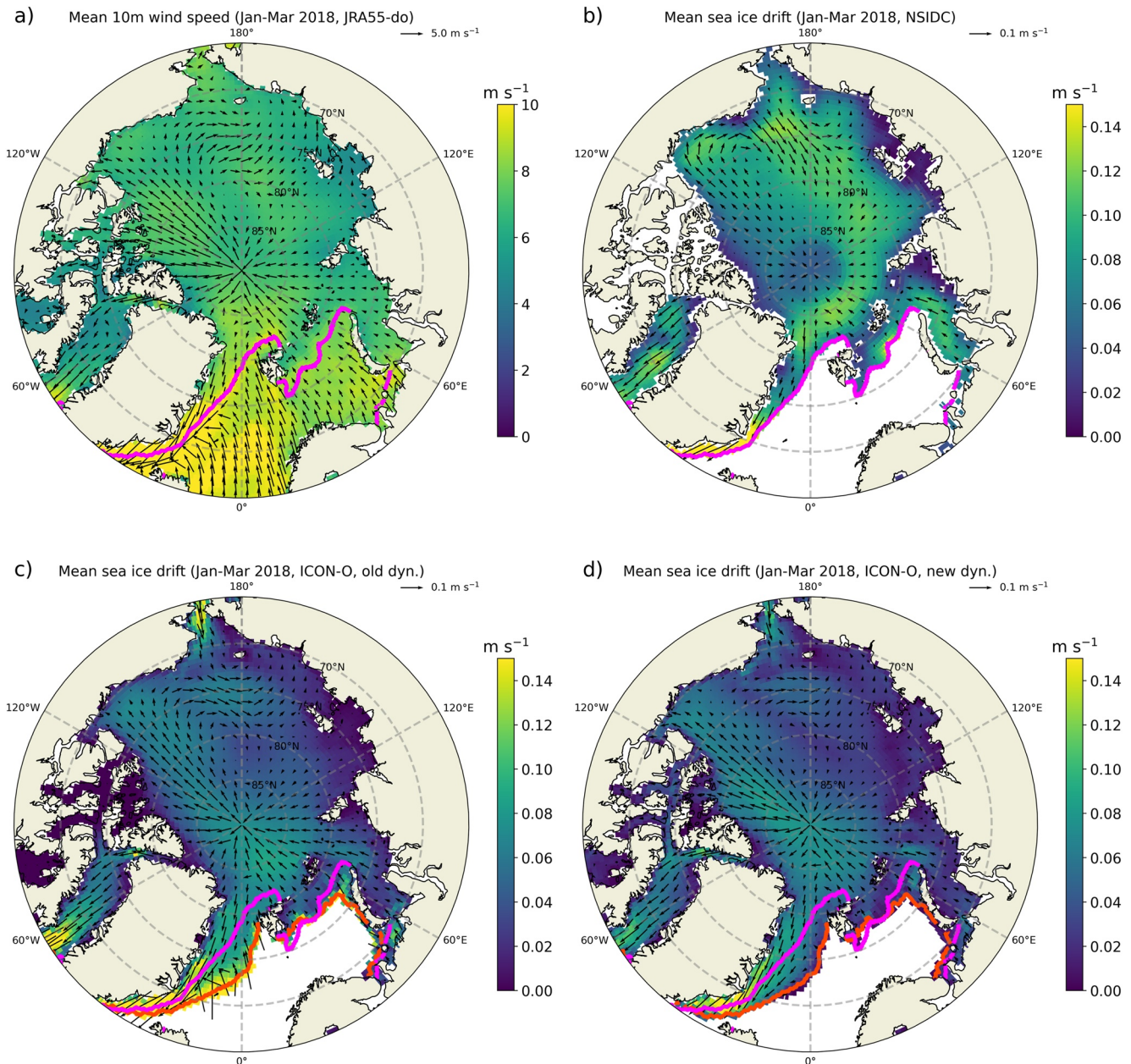
**Figure 5.** Mean (January–March 2018) (a) 10 m wind speed from JRA55-do and sea ice drift from (b) National Snow and Ice Data Center, (c) Icosahedral Non-hydrostatic-Ocean model (ICON-O) with the old sea ice dynamics, and (d) ICON-O with the new dynamics. The magenta contour marks the 15% sea ice concentration from Ocean and Sea Ice Satellite Application Facility (Lavergne et al., 2019) and the orange line the 15% sea ice concentration from ICON-O.

Overall, the large-scale sea ice drift simulated by ICON-O is reasonable given the wind forcing and similar when using the old or new sea ice dynamics.

## 5. Discussion and Conclusion

The paper presents an approximation of the sea ice dynamics in tangent planes to the sphere. The approximation can be applied to sea ice models discretized on grids in a three-dimensional Cartesian coordinate system. The concept is of particular interest for sea ice modules coupled to ocean models with a local coordinate system embedded in a three-dimensional Cartesian coordinate system, for example, ICON-O (Korn, 2017) or MPAS-O (Petersen et al., 2019).

The discretization is realized in the framework of the ocean model ICON-O and approximates the sea ice drift in two-dimensional reference systems. In each triangle, sea ice dynamics are approximated using a CD-grid-type approach (Mehlmann & Korn, 2021) that allows direct coupling to a C-grid discretization of the ocean. Based on a set of idealized test cases, we show the numerical robustness of the new approach and the first-order convergence of the discretization in space. The first-order convergence in space is expected because the CD-grid discretization is based on linear finite elements (Hansbo & Larson, 2003). Using ICON-O we demonstrate that the new numerical representation can capture the observed sea ice drift.

A benchmark comparison demonstrates that the CD-grid discretization is able to resolve the deformation structure of the sea ice cover better than the currently used discretizations (Mehlmann et al., 2021). As this deformation structure in the VP sea ice model begins to emerge at high mesh resolution, our future work will focus on analyzing the CD-grid approach at high spatial resolution in ICON-O.

## Data Availability Statement

The source code of the CD-grid implementation used for the numerical examples as well as the data sets for this research and the routines to process it are freely available from Mendeley Data (https://data.mendeley.com/datasets/2v5shnnmwx/3, Mehlmann, 2022). The model code of ICON is available to individuals under licenses (https://mpimet.mpg.de/en/science/modeling-with-icon/code-availability). By downloading the ICON-O source code, the user accepts the license agreement. The ICON-O simulations were conducted with the icon-oes "trr181ice" branch on https://gitlab.dkrz.de/icon/icon-oes in revision cb3ba5d4. The OSI SAF (Version 2.0, OSI-450) data were retrieved from https://thredds.met.no/thredds/osisaf/osisaf_cdrseaiceconc.html (last access date: 7 June 2022) (OSI SAF, 2017). The JRA55-do (Version 1.4.0) data were retrieved from http://esgf-data.dkrz.de/search/input4mips-dkrz/?mip_era=CMIP6%26activity_id=input4MIPs%26institution_id=MRI%26target_mip=OMIP%26source_id=MRI-JRA55-do-1-4-0 (last access date: 6 August 2021) (Tsujino et al., 2019). The monthly NSIDC mean sea-ice motion vectors (Version 4.1) were retrieved from https://doi.org/10.5067/INAWUWO7QH7B (last access date: 7 June 2022) (Tschudi et al., 2019).

## References

Comblen, S., ans Legrand, R., Deleersnijder, E., & Legat, V. (2009). A finite element method for solving the shallow water equations on the sphere. *Ocean Modelling*, 28(1), 12–23. https://doi.org/10.1016/j.ocemod.2008.05.004

Connolley, W. M., Gregory, J. M., Hunke, E., & McLaren, A. J. (2004). On the consistent scaling of terms in the sea-ice dynamics equation. *Journal of Physical Oceanography*, 34(7), 1776–1780. https://doi.org/10.1175/1520-0485(2004)034<1776:otcsot>2.0.co;2

Crouzeix, M., & Raviart, P.-A. (1974). Conforming and nonconforming finite element methods for solving the stationary Stokes equations. *Revue française d'automatique informatique recherche opérationelle. Mathématique*, 7(3), 33–76. https://doi.org/10.1051/m2an/197307r300331

Danilov, S., Sidorenko, D., Wang, Q., & Jung, T. (2017). The finite-volume sea ice–ocean model (FESOM2). *Geoscientific Model Development*, 10(2), 765–789. https://doi.org/10.5194/gmd-10-765-2017

Danilov, S., Wang, Q., Timmermann, R., Iakovlev, N., Sidorenko, D., Kimmritz, M., et al. (2015). Finite-Element Sea Ice Model (FESIM), version 2. *Geoscientific Model Development*, 8(6), 1747–1761. https://doi.org/10.5194/gmd-8-1747-2015

Falk, R. (1991). Nonconforming finite element Methods for the equations of linear elasticity. *Mathematics of Computation*, 57(196), 529–550. https://doi.org/10.1090/s0025-5718-1991-1094947-6

Guo, H. (2020). Surface Crouzeix–Raviart element for the Laplace–Beltrami equation. *Numerische Mathematik*, 144(3), 527–551. https://doi.org/10.1007/s00211-019-01099-7

Hansbo, P., & Larson, M. (2003). Discontinuous Galerkin and the Crouzeix–Raviart element: Application to elasticity. *ESAIM*, 37(1), 63–72. https://doi.org/10.1051/m2an:2003020

Hibler, W. (1979). A dynamic thermodynamic sea ice model. *Journal of Physical Oceanography*, 9(4), 815–846. https://doi.org/10.1175/1520-0485(1979)009<0815:adtsim>2.0.co;2

Hunke, E. (2001). Viscous-plastic sea ice dynamics with the EVP model: Linearization issues. *Journal of Computational Physics*, 170(1), 18–38. https://doi.org/10.1006/jcph.2001.6710

Hunke, E., & Dukowicz, J. (2002). The elastic–viscous–plastic sea ice dynamics model in general orthogonal curvilinear coordinates on a sphere—Incorporation of metric terms. *Monthly Weather Review*, 130(7), 1848–1865. https://doi.org/10.1175/1520-0493(2002)130<1848:TEVPSI>2.0.CO;2

Jungclaus, J., Lorenz, S. J., Schmidt, H., Brovkin, V., Brüggemann, N., Chegini, F., et al. (2021). The ICON earth system model version 1.0. *Journal of Advances in Modelling Earth Systems*, 14(4), e2021MS002813. https://doi.org/10.1029/2021MS002813

Korn, P. (2017). Formulation of an unstructured grid model for global ocean dynamics. *Journal of Computational Physics*, 339, 525–552. https://doi.org/10.1016/j.jcp.2017.03.009

Korn, P., Brüggemann, N., Jungclaus, J., Lorenz, S., Gutjahr, O., Haak, H., et al. (2022). ICON-O: The ocean component of the ICON Earth System Model—Global simulation characteristics and local telescoping capability. *Journal of Advances in Modeling Earth Systems*, 14(10), e2021MS002952. https://doi.org/10.1029/2021MS002952

Kreyscher, M., Harder, M., Lemke, P., Flato, G., & Gregory, M. (2000). Results of the Sea Ice Model Intercomparison Project: Evaluation of sea ice rheology schemes for use in climate simulations. *Journal of Geophysical Research*, 105(C5), 11299–11320. https://doi.org/10.1029/1999JC000016

Large, W. G., & Yeager, S. G. (2009). The global climatology of an interannually varying air-sea flux data set. *Climate Dynamics*, *33*(2–3), 341–364. https://doi.org/10.1007/s00382-008-0441-3

Lavergne, T., Sørensen, A. M., Kern, S., Tonboe, R., Notz, D., Aaboe, S., et al. (2019). Version 2 of the EUMETSAT OSI SAF and ESA CCI sea-ice concentration climate data records. *The Cryosphere*, *13*(1), 49–78. https://doi.org/10.5194/tc-13-49-2019

Lietaer, O., Fichefet, T., & Legat, V. (2008). The effects of resolving the Canadian Arctic Archipelago in a finite element sea ice model. *Ocean Modelling*, *24*(3–4), 140–152. https://doi.org/10.1016/j.ocemod.2008.06.002

Mehlmann, C. (2022). Sea ice dynamics in ICON-O—Numerical evaluation (version 3) [Dataset]. Mendeley Data. http://dx.doi.org/10.17632/2v5shnnmwx

Mehlmann, C., Danilov, S., Losch, M., Lemieux, J. F., Hutter, N., Richter, T., et al. (2021). Simulating linear kinematic features in viscous-plastic Sea Ice models on quadrilateral and triangular grids with different variable staggering. *Journal of Advances in Modeling Earth Systems*, *13*(11), e2021MS002523. https://doi.org/10.1029/2021MS00252

Mehlmann, C., & Korn, P. (2021). Sea-ice dynamics on triangular grids. *Journal of Computational Physics*, *428*, 110086. https://doi.org/10.1016/j.jcp.2020.110086

Notz, D., Haumann, F. A., Haak, H., Jungclaus, J., & Marotzke, J. (2013). Arctic sea-ice evolution as modeled by Max-Planck-Institute for Meteorology's Earth system model. *Journal of Advances in Modeling Earth Systems*, *5*(2), 173–194. https://doi.org/10.1002/jame.20016

OSI SAF. (2017). Global sea ice concentration climate data record v2.0—Multimission (version 2.0) [Dataset]. EUMETSAT SAF on Ocean and Sea Ice. http://dx.doi.org/10.15770/EUM_SAF_OSI_0008

Petersen, M., Asay-Davis, X., Berres, A., Chen, Q., Feige, N., Hoffman, M., et al. (2019). An evaluation of the ocean and sea ice climate of E3SM using MPAS and interannual CORE-II forcing. *Journal of Advances in Modeling Earth Systems*, *11*(5), 1438–1458. https://doi.org/10.1029/2018MS001373

Ringler, T., Petersen, M., Higdon, R., Jacobsen, D., Maltrud, M., & Jones, P. (2013). A multi-resolution approach to global ocean modelling. *Ocean Modelling*, *69*, 211–232. https://doi.org/10.1016/j.ocemod.2013.04.010

Semtner, A. (1976). A model for the thermodynamic growth of sea ice in numerical investigations of climate. *Journal of Physical Oceanography*, *6*(3), 379–389. https://doi.org/10.1175/1520-0485(1976)006<0379:amfttg>2.0.co;2

Steele, M., Morley, R., & Ermold, W. (2001). PHC: A global ocean hydrography with a high quality Arctic Ocean. *Journal of Climate*, *14*(9), 2079–2087. https://doi.org/10.1175/1520-0442(2001)014⟨2079:PAGOHW⟩2.0.CO;2

Stroeve, J., & Notz, D. (2018). Changing state of Arctic sea ice across all seasons. *Environmental Research Letters*, *13*(10), 103001. https://doi.org/10.1088/1748-9326/aade56

Tschudi, M., Meier, W. N., Stewart, J. S., Fowler, C., & Maslanik, J. (2019). Polar pathfinder daily 25 km EASE-grid Sea Ice Motion vectors, version 4.1 [Dataset]. NASA National Snow and Ice Data Center Distributed Active Archive Center. http://dx.doi.org/10.5067/INAWUWO7QH7B

Tsujino, H., Urakawa, S., Nakano, H., Small, R. J., Kim, W. M., Yeager, S. G., et al. (2018). JRA-55 based surface dataset for driving ocean–sea-ice models (JRA55-do). *Ocean Modelling*, *130*, 79–139. https://doi.org/10.1016/j.ocemod.2018.07.002

Tsujino, H., Urakawa, S., Nakano, H., Small, R. J., Kim, W. M., Yeager, S. G., et al. (2019). input4MIPs.CMIP6.OMIP.MRI.MRI-JRA55-do-1-4-0 (version 1.4.0) [Dataset]. Earth System Grid Federation. http://dx.doi.org/10.22033/ESGF/input4MIPs.10842

Wang, Q., Danilov, S., Sidorenko, D., Timmermann, R., Wekerle, C., Wang, X., et al. (2014). The Finite Element Sea Ice-Ocean Model (FESOM) v.1.4: Formulation of an ocean general circulation model. *Geoscientific Model Development*, *7*(2), 663–693. https://doi.org/10.5194/gmd-7-663-2014